mater.scichina.com link.springer.com

Published online 15 September 2022 | https://doi.org/10.1007/s40843-022-2172-6
Sci China Mater 2022, 65(12): 3382–3391

SPECIAL ISSUE: Energy Transitions towards Carbon Neutrality

Synergistic high efficiency and low energy loss of all-small-molecule organic solar cells based on benzotriazole-based π-bridge unit

Jing Guo[1,2], Ke Hu[1,2], Beibei Qiu[3*], Dengchen Yang[1,2], Xiaojun Li[1,2], Jinyuan Zhang[2*], Lei Meng[1,2*], Zhanjun Zhang[1*] and Yongfang Li[1,2,4]

ABSTRACT **Reducing energy loss (V_{loss}) is one of the most crucial challenges in organic photovoltaic cells. The V_{loss}, determined by the differences between the optical band gap (E_g) of the active layer material and the open-circuit voltage (V_{oc}) of the device, is generally alleviated by lowering the energy difference between the lowest unoccupied molecular orbital (LUMO) and highest occupied molecular orbital (HOMO) level of the donor (D) and acceptor (A). In this work, we synthesized two A-π-D-π-A-type small-molecule donors (SMDs) SM-benzotriazole (BTz)-1 and SM-BTz-2 by introducing a BTz π-bridge unit and terminal regulation. The BTz π-bridge unit significantly lowers the HOMO energy level of SMDs, resulting in high V_{oc} and high mobility, achieving a balance of low energy loss (<0.5 eV) and high efficiency. Ultimately, the organic solar cells based on SM-BTz-2 as the donor and Y6 as the acceptor obtain a high V_{oc} of 0.91 V, J_{sc} of 22.8 mA cm^{-2}, fill factor of 68%, and power conversion efficiency (PCE) of 14.12%, which is one of the highest efficiencies based on the SMDs with triazole π-bridges to date. What's more, the BTz π-bridge unit is a potential unit that can improve mobility and reduce energy loss.**

Keywords: small-molecule donor materials, all-small-molecule organic solar cells, benzotriazole π-bridge, energy loss

INTRODUCTION

Bulk heterojunction organic solar cells (OSCs) have gotten attention on account of their low cost, lightweight, and capacity for preparing large-area flexible devices in recent years [1–6]. The typical OSCs' active layers consist of donor and acceptor materials (mainly polymers and small molecules). Recently, the binary or ternary single-junction OSCs built on conjugated polymer donors and non-fullerene small-molecule acceptors have achieved remarkable breakthroughs, with the power conversion efficiency (PCE) of over 18% [7–11]. However, batch variation of polymers is unavoidable and maybe limits the reproducibility of the device photovoltaic performance, and thus all-small-molecule OSCs (SM-OSCs) have received more and more attention because of their advantages of easy purification, clear chemical structure and molecular weight, and small differences between batches [12–15].

With the development of small-molecule photovoltaic materials, the PCEs of the most advanced SM-OSCs have achieved over 16%, indicating the considerable potential for practical applications. Nevertheless, SM-OSCs still face the challenge of the relatively large energy loss (E_{loss}) compared with silicon and perovskite solar cells, which is a critical factor restricting the further development of OSCs. It has been recognized that reducing the E_{loss} is one of the main pathways to promoting the PCEs. The E_{loss} equals to $E_g - qV_{oc}$, where E_g is the optical bandgap of the active layer, V_{oc} is the open-circuit voltage of the devices, and q is the elementary charge [16]. V_{oc} is positively correlated with the difference between the highest occupied molecular orbital (HOMO) energy level of the donor and the lowest unoccupied molecular orbital (LUMO) energy level of the acceptor. There have been many reports on the E_{loss} of polymer solar cells (PSCs), but the low E_{loss} and high-efficiency systems of SM-OSCs are rarely reported. This is partly because a small energy loss usually requires a low energetic offset between the donor and acceptor, which may lead to an insufficient driving force for exciton dissociation, making the trade-off between the photovoltaic performance and energy loss of devices a momentous study focus. Generally, one strategy to address this problem is to incorporate a third component with a deeper HOMO level donor [17,18] or a shallower LUMO level acceptor into the binary host matrix to modulate the energy level of the active layers, constructing a ternary system with low energy loss [19,20], and the other is developing a binary system with low energy loss without sacrificing the PCE [21,22].

[1] School of Chemical Science, University of Chinese Academy of Sciences, Beijing 100049, China
[2] Beijing National Laboratory for Molecular Sciences, CAS Key Laboratory of Organic Solids, Institute of Chemistry, Chinese Academy of Sciences, Beijing 100190, China
[3] Key Laboratory of Solid State Optoelectronic Devices of Zhejiang Province, College of Physics and Electronic Information Engineering, Zhejiang Normal University, Jinhua 321004, China
[4] Laboratory of Advanced Optoelectronic Materials, Suzhou Key Laboratory of Novel Semiconductor-optoelectronics Materials and Devices, College of Chemistry, Chemical Engineering and Materials Science, Soochow University, Suzhou 215123, China
* Corresponding authors (emails: qiubeibei@zjnu.edu.cn (Qiu B); zhangjinyuan@iccas.ac.cn (Zhang J); menglei@iccas.ac.cn (Meng L); zhangzj@ucas.ac.cn (Zhang Z))

High-efficiency small-molecule donor (SMD) materials are generally the typical A-π-D-π-A structures, that is, consisting of an electron-donor group (D) as a core building block and two electron-deficient units (A) as the end groups with a π electron linkage unit for efficient modulation of the effective conjugation length and stacking mode of the molecules [23–25]. A conjugated system benzodithiophene (BDT) with good planarity and superior charge transport properties is usually used as the central D-unit with side chain groups to regulate the molecular solubility, molecular energy levels, optical absorption and molecular aggregation state. To improve the photoelectric properties of the molecules, many studies have been carried out to alter the side chains, π-bridges, and/or the ending A-units [26–29]. Chen's group [30] synthesized an SMD DRTB-FT with a low-lying HOMO energy level *via* introducing fluorine atoms into the thiophene side chain substituent of the donor central BDT unit. The PCE of the SM-OSC based on DRTB-FT:F-2Cl is 7.66%, V_{oc} is 1.070 V, and E_{loss} is 0.47 eV, while the mismatched carrier mobilities of the device and the inferior morphology of the blend film result in low J_{sc} and fill factor (FF).

Different π-bridge configurations, such as thieno[3,2-*b*]thiophene (TT) [31,32], benzo[1,2-*c*:4,5-*c*′]dithiophene-4,8-dione (BDD) [33], halogenated phenyl [34] and other π bridges, could form different molecular backbone configurations, which can optimize the photovoltaic performance. Recently, Zhang's group [35] designed and synthesized a broad-gap SMD BTTzR using an electron-deficient thiazoline-[5,4-*d*]thiazoline-thiophene (TTz) unit as the π-bridge unit, and combined with the acceptor Y6 to obtain a PCE of 13.9% and an E_{loss} of 0.51 eV, which is equivalent to the E_{loss} of inorganic solar cells.

The benzotriazole (BTz) unit has also been broadly used for the construction of donor photovoltaic materials combined with electron-donating D-units, benefiting from their planar-ordered packing structure and high carrier mobilities. In addition, due to the electron-deficiency characteristic of BTz, the HOMO level of the donor with BTz as A-unit is lower, resulting in higher V_{oc} and lower E_{loss} of the device. The BTz-containing PSCs exhibit excellent performance with high V_{oc} [36–38]. In a previous study, Bin *et al.* [39,40] synthesized a variety of wide-bandgap small-molecule donors by introducing a BTz unit as π-bridge, which has high photovoltaic performance, thanks to its planar structure easy to form ordered π-stacking and high hole mobility. Here, two new A-π-D-π-A structured SMDs, SM-BTz-1 and SM-BTz-2 were synthesized with BDT-TS (benzodithiophene with alkylthiosubstituted thiophene unit) as the D core, a difluoro-substituted BTz with two thiophene units as the electron-deficient unit (π-bridge) and rhodamines with different lengths as the A end groups. The two SMDs show enhanced absorption coefficients, lower HOMO energy levels and higher hole mobilities. The SM-OSC with SM-BTz-2 as the donor and Y6 as the acceptor enables a high efficiency of 14.12%, accompanied by a high V_{oc} of 0.91 V, a short-circuit current density (J_{sc}) of 22.8 mA cm^{-2} and an FF of 0.68, which is one of the highest efficiencies for the SM-OSCs based on the SMD with BTz π bridges, simultaneously achieving high efficiency and low energy loss.

RESULTS AND DISCUSSION

The synthetic procedures of SM-BTz-1 and SM-BTz-2 are shown in Fig. 1a. Fig. 1b and Fig. S1 show the ultraviolet-visible absorption spectra of the SMDs SM-BTz-1 and SM-BTz-2, and the acceptor Y6, in solid films and dilute chloroform solutions, respectively. SM-BTz-1 and SM-BTz-2 exhibit almost identical absorption profiles in solution, with the maximum absorption (λ_{abs}^{max}) peak at 524 and 527 nm, respectively. Besides, from the temperature-dependent absorption measurements, the absorption curve undergoes a slight blue shift when the solution temperature warmed from 0 to 60°C. However, the film absorptions of SM-BTz-1 and SM-BTz-2 are red-shifted, with main peaks at 562 nm for SM-BTz-1 and 566 nm for SM-BTz-2 relative to the solution peaks, which should be due to the different aggregation properties. Furthermore, SM-BTz-2 has a stronger shoulder peak at 618 nm, which shows strong molecular aggregation and intermolecular interactions in the SM-BTz-2 film. The absorption edges of SM-BTz-1 and SM-BTz-2 films are located at 687 and 697 nm, and the corresponding optical band gaps (E_g^{opt}) are 1.49 and 1.47 eV, respectively, indicating a favorable absorption complementary with the acceptor Y6. Taken together, the above results demonstrate that SM-BTz-1 and SM-BTz-2 have good solubility in chloroform and excellent conformational and morphological stability in the film state.

We performed cyclic voltammetry (CV) to determine the electrochemical energy levels of the two donor films. The initial oxidation/reduction potentials ($\varphi_{ox}/\varphi_{red}$) of SM-BTz-1 and SM-BTz-2 were obtained from the CV as 1.15/−0.69 and 1.13/−0.68 V *vs.* Ag/Ag$^+$, respectively (Fig. S2). The redox potential of Fc/Fc$^+$ relative to Ag/Ag$^+$ reference electrode was 0.44 V. Hence, according to the formula HOMO/LUMO = $-e(\varphi_{ox}/\varphi_{red} + 4.36)$ (eV), the HOMO/LUMO levels of SM-BTz-1 and SM-BTz-2 were −5.51/−3.67 and −5.49/−3.68 eV, respectively (Fig. 1c and Table 1). The V_{oc} of OSCs was positively correlated with the difference between the donor HOMO energy level and the acceptor LUMO energy level [41]. Therefore, the relatively low HOMO levels of the donors SM-BTz-1 and SM-BTz-2 favor the higher V_{oc} obtained from SM-OSCs. Furthermore, both HOMO (−5.65 eV) and LUMO (−4.10 eV) energy levels of the acceptor Y6 are lower than those of SM-BTz-1 and SM-BTz-2, and the donor/acceptor energy levels match well, thereby effectively promoting the exciton dissociation and charge transport.

The geometric structures of SM-BTz-1 and SM-BTz-2 were theoretically calculated using density functional theory (DFT), and all the other alkyl chains except the terminal alkyl chain were substituted by methyl to simplify the calculation. The optimized geometries of SM-BTz-1 and SM-BTz-2 were shown in Fig. 2a, the dihedral angles between the main chain and side chain groups of the two molecules are very nearly the same, and the main difference lies in the end groups. Compared with SM-BTz-2 with the *n*-butyl alkyl chain at the end, SM-BTz-1 with 2-ethylhexyl alkyl chain end produces greater steric hindrance, which is harmful to the formation of tight molecular stacking and affects the carrier mobility.

As displayed in Fig. 2b, the differential scanning calorimetry (DSC) thermogram of SM-BTz-1 displays two endothermic peaks with melting enthalpies (ΔH_m) of 18.46 J g^{-1} at 255.6°C and 5.33 J g^{-1} at 289.9°C, respectively, and the corresponding exothermic peaks at 162 and 283°C, with the crystal enthalpy (ΔH_c) of 10.49 and 4.25 J g^{-1}. While SM-BTz-2 only presents a weak melting peak and crystallization peak at 224.9 and 194.4°C, respectively, and the corresponding enthalpies are 7.71 and 3.68 J g^{-1}, indicating that SM-BTz-2 is easier to form ordered

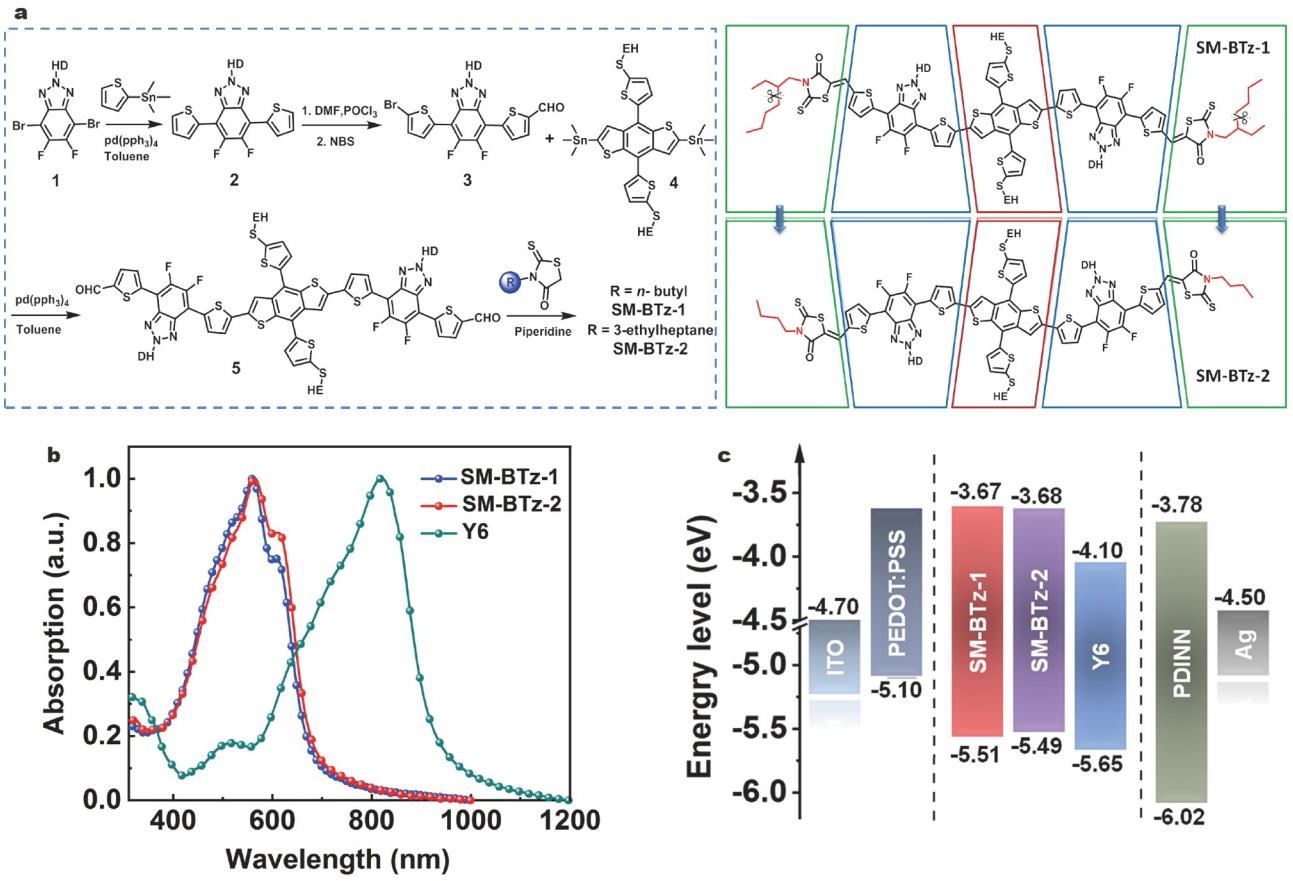

Figure 1 (a) The molecular structures and synthesis routes of SM-BTz-1 and SM-BTz-2. (b) The thin film ultraviolet-visible absorption spectra of SM-BTz-1 and SM-BTz-2, and the acceptor Y6. (c) Energy level diagram of SM-BTz-1, SM-BTz-2 and Y6.

Table 1 The detailed data of thermogravimetric, absorption spectrum and energy levels of SM-BTz-1 and SM-BTz-2

Donor	T_d (°C)	λ_{abs}^{max} (nm)		λ_{onset} film (nm)	E_g (eV)	E_{HOMO} (eV)	E_{LUMO} (eV)
		solution	film				
SM-BTz-1	346	524	562	687	1.49	−5.51	−3.67
SM-BTz-2	314	527	566	697	1.47	−5.49	−3.68

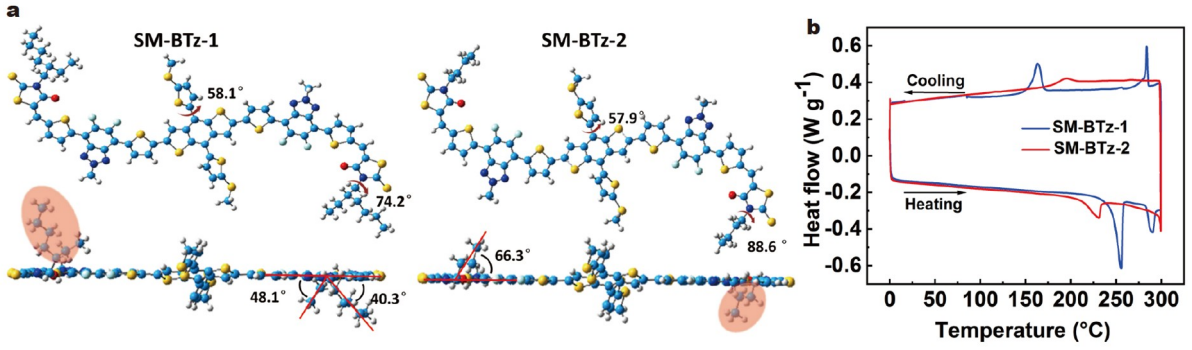

Figure 2 (a) Optimized geometric structures of the SMDs by DFT theoretical calculation. (b) DSC curves of the SMDs.

aggregation. In addition, in Fig. S3, high decomposition temperatures (T_d) of 346°C for SM-BTz-1 and 314°C for SM-BTz-2 with 5% weight loss are demonstrated *via* thermogravimetric analysis (TGA), displaying the superb thermal stability of SM-BTz-1 and SM-BTz-2 for the application in SM-OSCs.

Photovoltaic performance

The SM-OSCs with the traditional structure of indium tin oxide (ITO)/poly(3,4-ethylenedioxythiophene):poly(4-styrenesulfonate) (PEDOT:PSS)/SM-BTz-1:Y6 or SM-BTz-2:Y6/aliphatic amine-functionalized perylene-diimide (PDINN)/Ag [42,43]

were prepared to explore the photovoltaic performance of the two small-molecule donors. The active layers were spin-coated from chloroform blend solutions of SM-BTz-1:Y6 or SM-BTz-2:Y6. The device processing conditions, including thermal annealing (TA) temperature, annealing time and donor/acceptor weight ratios (Tables S1–S3) were carefully tuned to enhance the photovoltaic performance of SM-OSCs. The optimized current density-voltage (*J*-*V*) curves of the SM-OSCs based upon SM-BTz-1:Y6 and SM-BTz-2:Y6 (2:1, *w*/*w*) are shown in Fig. 3a, and the corresponding photovoltaic performance parameters are detailed in Table 2. The results show relatively poor as-cast device performance for the two small-molecule donors, with PCE below 5%, which ought to be attributed to the poor phase separation discussed later in the morphological analysis section. The J_{sc} and FF of the device, however, are dramatically improved after TA treatment, while the V_{oc} slightly decreases, which may be caused by the enhanced interaction between the donor and acceptor molecules. The best PCE of the devices is 14.12%, with a high V_{oc} of 0.91 V, J_{sc} of 22.8 mA cm^{-2}, and FF of 0.68 for the SM-BTz-2:Y6. Notably, the 0.91 V is one of the highest V_{oc} values for the Y6-based SM-OSCs. Besides, the external quantum efficiency (EQE) images show that the photoresponse values are wide and high in the SM-BTz-2:Y6 device, and especially at 460–830 nm, the EQE reaches more than 70%, indicating that the SM-OSC system exhibits efficient exciton dissociation and charge transport and collection. Meanwhile, the integrated value of J_{sc} calculated from the EQE curve is in agreement with the value of J_{sc} measured by *J*-*V*. In order to realize the future commercial application, both the stability of the photo-active material itself and the stability of the device structure (such as charge transport layer) should be carefully taken into consideration. We further studied the photostability of the two SM-OSCs devices. As shown in Fig. S4, the SM-OSCs still maintained more than 70% of their original PCEs after 300 h of continuous illumination. Amazingly, the V_{oc} of the two low energy loss systems are basically unchanged, and only the J_{sc} and FF decrease slightly, indicating that the system has good photostability.

To thoroughly investigate the exciton dissociation and charge collection processes of SM-OSCs, the dependence of the photocurrent (J_{ph}) on the applied voltage (V_{eff}) was measured, and the results are shown in Fig. 3c. Define J_{ph} as $J_L - J_D$, where J_L and J_D are the current densities under light and dark conditions, respectively. V_{eff} equals $V_0 - V$, where V_0 is the voltage when $J_{ph} = 0$, and V is the applied voltage. For both SM-OSCs, when the J_{ph} values reach the saturation current density (J_{sat}) at $V_{eff} \geq 2$ V, the probability of the charge dissociation $P(E, T)$ can be expressed as the J_{ph}/J_{sat} ratio, where E is the electric field and T is the temperature [44]. Under short-circuit and maximum power output conditions, the $P(E, T)$ of the SM-BTz-1-based and SM-BTz-2-based devices are 96.29% and 97.13%, respectively, revealing that the SM-BTz-2:Y6 device has sufficient exciton dissociation and more efficient charge extraction.

We evaluated the V_{oc} and J_{ph} values under different light

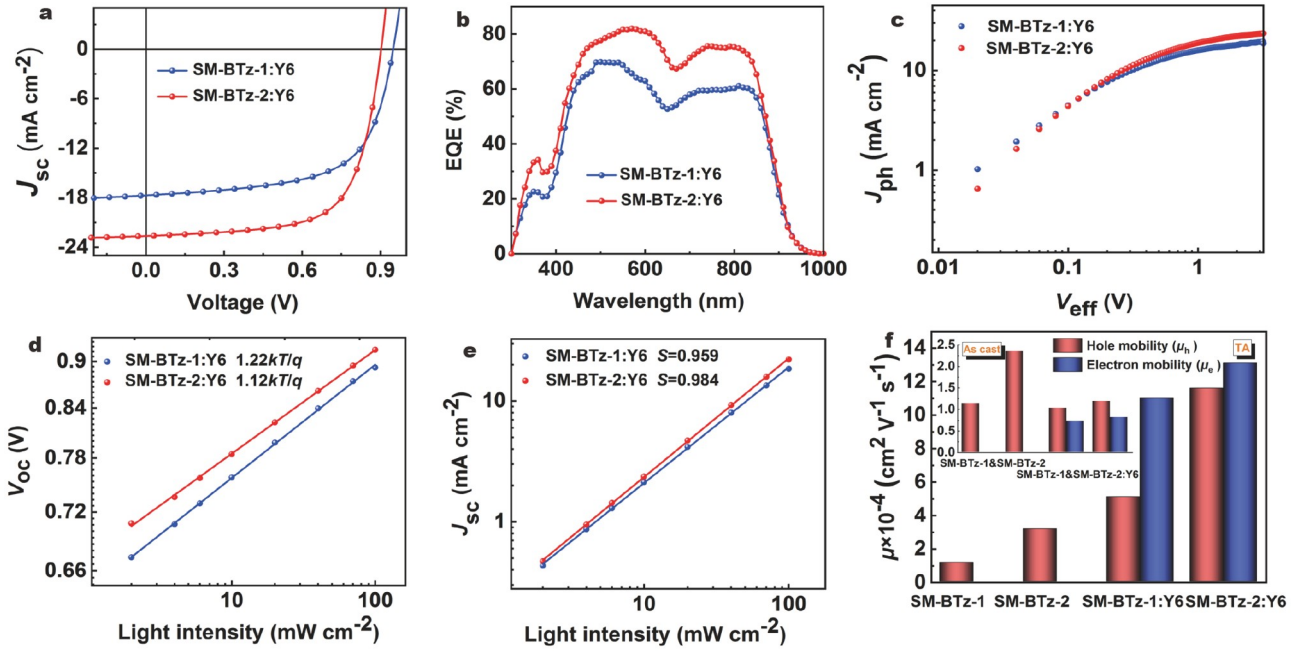

Figure 3 (a) *J*-*V* characteristic curves of the optimized SM-BTz-1:Y6 and SM-BTz-2:Y6 devices. (b) EQE curves of the SM-BTz-1:Y6 and SM-BTz-2:Y6 devices. (c) J_{ph} *versus* V_{eff} curves of the SM-OSCs. (d) Dependence of V_{oc} on P_{light} of the SM-OSCs. (e) Dependence of J_{sc} on P_{light} of the SM-OSCs. (f) Hole and electron mobilities of the SM-OSCs.

Table 2 Summary of photovoltaic parameters of the optimized SM-OSCs based on SMDs:Y6

SMDs	V_{oc} (V)	J_{sc} (mA cm^{-2})	FF (%)	PCE (%)	J_{sc}^{a} (mA cm^{-2})
SM-BTz-1	0.94 (0.932 ± 0.006)	17.76 (17.33 ± 0.43)	0.63 (0.631 ± 0.14)	10.52 (10.48 ± 0.19)	17.23
SM-BTz-2	0.91 (0.896 ± 0.005)	22.82 (22.56 ± 0.43)	0.68 (66.96 ± 0.22)	14.12 (14.16 ± 0.21)	22.37

a) The J_{sc} values are integrated from the EQE spectra.

intensities (P_{light}) to investigate the charge recombination behavior in SM-OSCs. The V_{oc} and P_{light} comply with the relationship: $V_{oc} \propto nkT/q\ln(P_{light})$, and the extent of bimolecular or trap-assisted recombination can be estimated by evaluating the slope of V_{oc} *vs.* $\ln(P_{light})$. More specifically, when the slope is $1kT/q$ or $2kT/q$, the recombination mechanism is bimolecular or trap-assisted recombination, respectively [42,45]. Herein, the slope of the SM-BTz-2:Y6 device is significantly lower at $1.12kT/q$, demonstrating that the trap-assisted recombination was effectively suppressed, and compared with the SM-BTz-1-based device, the SM-BTz-2-based device is predominated by bimolecular recombination. Additionally, the relation between J_{sc} and P_{light} obeys $J_{sc} \propto (P_{light})^S$ with the linear correlation between $\log(J_{sc})$ and $\log(P_{light})$ and the weaker the bimolecular recombination, the closer the S value is to 1. As shown in Fig. 3e, the S of the devices is 0.959 for SM-BTz-1:Y6 and 0.984 for SM-BTz-2:Y6, indicating that the bimolecular recombination of the SM-BTz-2:Y6 device is lower.

The carrier mobilities of the active layers were determined by the space charge confined current (SCLC) method, where the hole mobilities (μ_h) and electron mobilities (μ_e) of the active layers employed hole-only ITO/PEDOT:PSS/SM-BTz-1:Y6 or SM-BTz-2:Y6/MoO_3/Ag and electron-only ITO/ZnO/SM-BTz-1:Y6 or SM-BTz-2:Y6/PDINN/Ag device structure measurement, respectively. The results are shown in Fig. 3f, Fig. S5 and Table S4. Before TA treatment, both two blends present inferior charge mobilities. The μ_h of the SM-BTz-1:Y6 and the SM-BTz-2:Y6 in the binary blend films are 1.03×10^{-4} and 1.19×10^{-4} $cm^2\ V^{-1}\ s^{-1}$, and the corresponding μ_e are 7.30×10^{-5} and 8.16×10^{-5} $cm^2\ V^{-1}\ s^{-1}$, while the electron/hole mobilities ratio (μ_h/μ_e) values are 1.41 and 1.46, respectively. After TA treatment, the μ_h and μ_e of the blend films are significantly improved, especially for the μ_e, which is raised by two orders of magnitude, and the μ_e are 1.10×10^{-3} $cm^2\ V^{-1}\ s^{-1}$ for the SM-BTz-1:Y6 blend and 1.31×10^{-3} $cm^2\ V^{-1}\ s^{-1}$ for the SM-BTz-2:Y6 blend. More importantly, the SM-BTz-2:Y6 blend film has more balanced carrier mobility (μ_h/μ_e = 0.88). Therefore, the higher and more balanced carrier mobilities lead to the higher J_{sc} and FF values for the SM-BTz-2:Y6-based devices.

Compared with other reported SM-OSCs, this system presents relatively high V_{oc}, while excellent J_{sc} values are kept. To further explore the reason for the high V_{oc} in the SM-BTz-1 and SM-BTz-2:Y6-based device, the total energy loss (E_{loss}) was described by an equation:

$$\begin{aligned} E &= E_g - qV_{OC} \\ &= (E_g - qV_{OC}^{SQ}) + (qV_{OC}^{SQ} - qV_{OC}^{rad}) + (qV_{OC}^{rad} - qV_{OC}) \\ &= E_1 + E_2 + E_3. \end{aligned}$$

The ΔE_1 is the inevitable radiation energy loss, which is caused by the difference between E_g and the theoretical maximum voltage (V_{OC}^{SQ}) multiplied by the elementary charge [46,47]. The V_{OC}^{SQ} can be calculated according to the Shockley-Queisser (SQ) limit, which assumes ideal absorption above the E_g [48]. The ΔE_2 is the additional radiation compound loss due to the absorption below the band gap. The $q\Delta V_{nr}$ comes from the non-radiative recombination, which can be calculated as $\Delta E_3 = q\Delta V_{nr} = -kT\ln(EQE_{EL})$, where k is the Boltzmann constant and T is Kelvin temperature [49]. Fig. 4a, b show the intersection of the normalized electroluminescence (EL) spectrum and EQE spectra, and the optical bandgap values of SM-BTz-1:Y6 and SM-BTz-2:Y6 were calculated as 1.41 and 1.40 eV, respectively. Therefore, the total E_{loss} values of the SM-BTz-1:Y6 and SM-BTz-2:Y6 are determined to be 0.478 and 0.499 eV, respectively. The specific energy losses based on SM-BTz-1:Y6 and SM-BTz-2:Y6 are

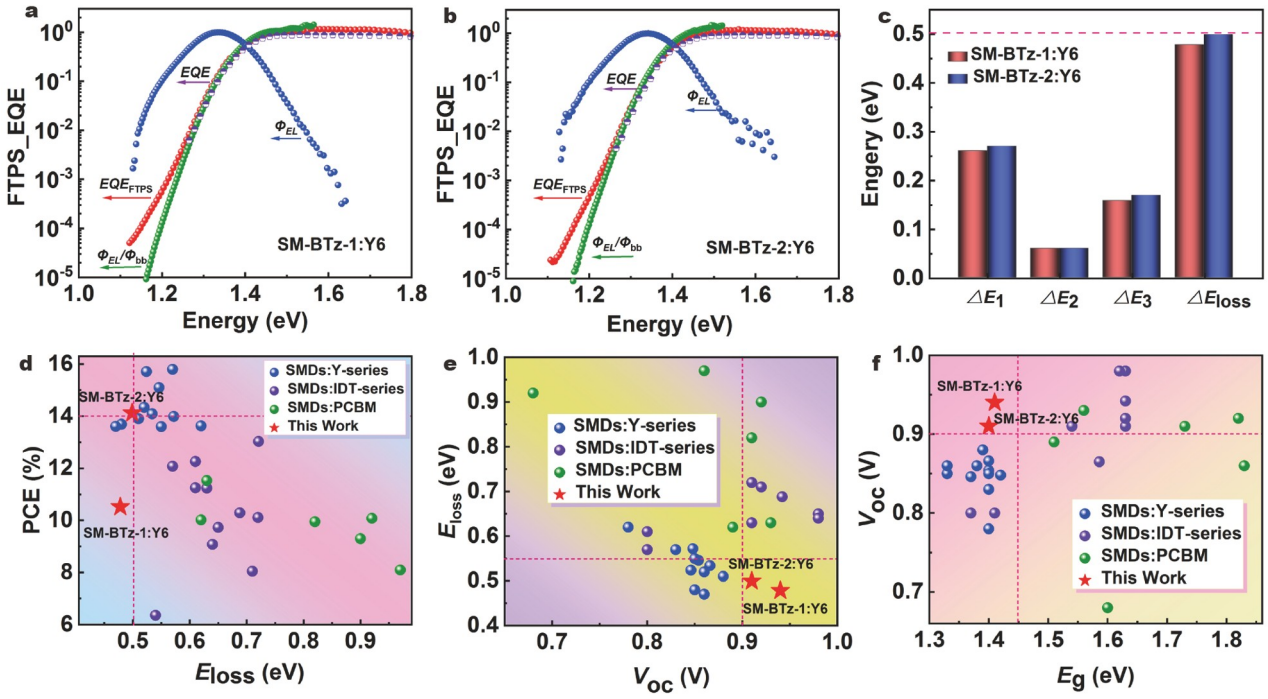

Figure 4 (a, b) Fourier transform photocurrent spectroscopy (FTPS)-EQE, EQE, normalized EL, and $\varphi_{EL}/\varphi_{bb}$ of the SM-BTz-1:Y6 and SM-BTz-2:Y6 devices. (c) Summary of the energy losses of the SM-BTz-1:Y6 and SM-BTz-2:Y6 devices. Statistics of the relevant parameters of SM-OSCs in recent years: (d) PCE *vs.* energy loss (E_{loss}), (e) E_{loss} *vs.* V_{oc} and (f) V_{oc} *vs.* E_g.

summarized in Fig. 4c, and Table S5. The ΔE_1 was determined to be 0.260 eV and ΔE_2 to be 0.060 eV for SM-BTz-1:Y6 and the ΔE_1 and ΔE_2 of SM-BTz-2:Y6 to be 0.270 and 0.060 eV, respectively. As shown in Fig. S6, the ΔE_3 corresponding to SM-BTz-1:Y6 and SM-BTz-2:Y6 devices was calculated based on EQE_{EL} values to be 0.158 and 0.169 eV, respectively.

It is worth noting that the E_{loss} of the devices based on SM-BTz-1:Y6 and SM-BTz-2:Y6 are both less than 0.5 eV, which are lower than those of other reported SM-OSCs (Fig. 4d–f, and Table S6). Especially, the non-radiative energy losses (ΔE_3) are very low, so that the SM-BTz-1 and SM-BTz-2:Y6-based devices achieve the PCE of 10.52% and 14.12% with the high V_{oc} of 0.94 and 0.91 V. For all we know, the V_{oc} of 0.91 V is one of the highest values of the binary SM-OSCs with PCE over 14%. The results display that questing high V_{oc} while maintaining well J_{sc} and FF is a favorable way to achieve high-performance SM-OSCs.

We adopted transmission electron microscopy (TEM) to detect the single-component film morphology of the two donors and acceptor (Y6) before and after TA treatment. As shown in the image in Fig. 5, the dark and bright regions of the acceptor Y6 before and after annealing are large, the molecular agglomeration is obvious, and the boundaries are blurred. The intrinsic properties of the two small molecules can be clearly observed before TA treatment, and the SM-BTz-1 image presents branched hierarchies in dark regions. On the other hand, SM-BTz-2 shows a denser and smoother morphology after annealing treatment compared with SM-BTz-1.

Moreover, the atomic force microscopy (AFM) and TEM measurements were also performed to further learn about the morphology of the blend active layer. From the AFM images (Fig. 6a, b), it can be seen that the RMS roughness values of the as-cast SM-BTz-1:Y6 and SM-BTz-2:Y6 blend films are 1.65 and 2.49 nm, respectively. After the TA treatment, RMS values are significantly reduced to 1.50 and 1.44 nm, respectively. Furthermore, the clear smooth surface means better molecular stacking orderliness, which is conducive to obtaining a higher J_{sc} and FF after TA treatment. In the TEM images, SM-BTz-1:Y6 blends have little difference before and after TA treatment, and irregular mosaic patterns are formed in the whole image. However, SM-BTz-2:Y6 blends possess smaller phase separation aggregates after annealing treatment. Compared with the single component films, SM-BTz-2:Y6 blends have more obvious and uniform light and dark distribution morphology, and the distance between the dark and bright area is about tens of nanometers, which is in favor of facilitating the exciton dissociation and carrier transport, enhancing the J_{sc} and FF.

The morphologies of SM-BTz-1 and SM-BTz-2 and the binary blend films were measured by grazing incidence wide-angle X-ray scattering (GIWAXS). Fig. 7, Tables S7 and S8 show the two-dimensional (2D) GIWAXS images of pure and blended films under optimal conditions, the corresponding scattering profiles, and associated calculations. The out-of-plane (OOP) profiles of the pure SM-BTz-1 and SM-BTz-2 films show conspicuous (100) diffraction peaks at 0.284 $Å^{-1}$ ($d \approx 22.124$ Å) and 0.288 $Å^{-1}$ ($d \approx 21.817$ Å), respectively, which means that the SM-BTz-2 film possesses the tighter packing characteristic. Similar results could also be obtained from the in-plane (IP) profiles. The strong (010) diffraction peaks locate at ~1.736 and 1.757 $Å^{-1}$, corresponding to the π-π stacking of SM-BTz-1 and SM-BTz-2 with a d-spacing of 3.619 and 3.576 Å, respectively. These results imply that the SM-BTz-1 and SM-BTz-2 films tend to adopt an edge-on dominant orientation. The Y6 neat film shows clear (100) diffraction peaks at 0.320 $Å^{-1}$ in the IP direction and an apparent (010) π-π stacking diffraction peak at 1.715 $Å^{-1}$ in the OOP direction with the corresponding d of 3.664 Å. Furthermore, the neat Y6 film is inclined to a face-on molecular orientation, leading to the peak intensities of blend films significantly improved compared with the pure films for both the (100) and (010) packing planes, which corresponds to the increase in crystallinity of SM-BTz-1 and SM-BTz-2 (see Fig. S7). Therefore, the blend films have strong face-on and

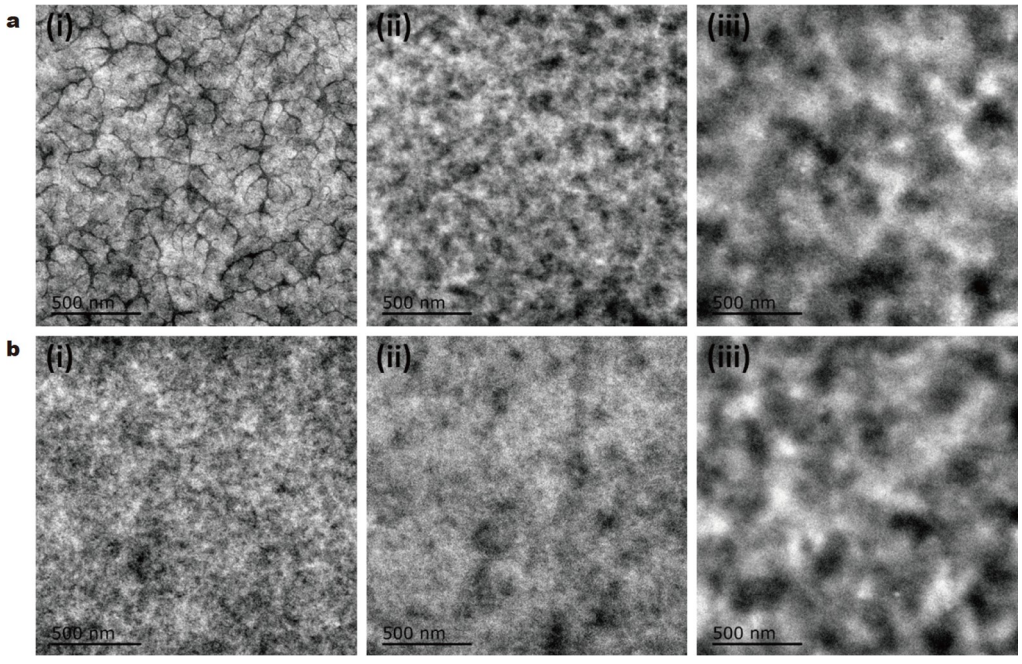

Figure 5 TEM images of neat films: (i) SM-BTz-1 film, (ii) SM-BTz-2 film, (iii) Y6 film. (a) As-cast films, and (b) TA-treated films at 120°C for 5 min.

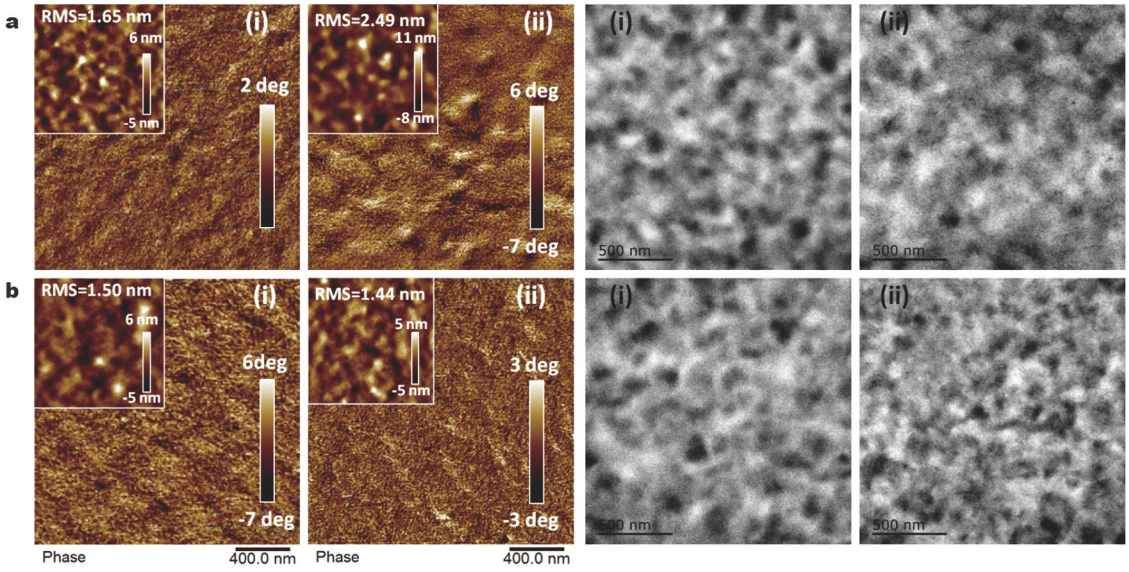

Figure 6 AFM and TEM images of (i) SM-BTz-1:Y6 blend film, (ii) SM-BTz-2:Y6 blend film. (a) As-cast films; (b) TA-treated films at 120°C for 5 min.

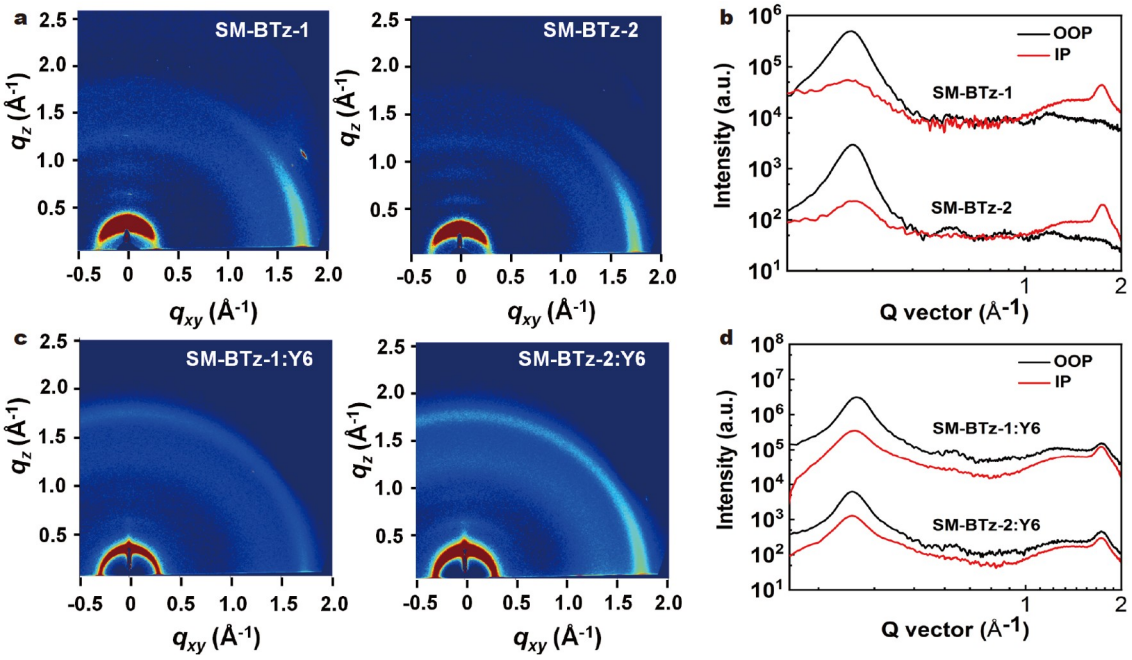

Figure 7 (a) 2D GIWAXS patterns for the SM-BTz-1 and SM-BTz-2 neat films. (c) 2D GIWAXS patterns for the SM-BTz-1:Y6 and SM-BTz-2:Y6 blend films under optimized conditions. (b, d) 1D line-cut contours corresponding to the OOP (dark) and IP (red) directions of the films.

edge-on mixed molecular orientations. Moreover, according to the Scherrer equation [50,51], the crystal coherence length (CCL) was calculated by fitting the maximum half-width of the (100) diffraction peak and the (010) diffraction peak. Relative to the SM-BTz-1:Y6 blend films, the CCLs (100) and (010) of the SM-BTz-2:Y6 blend films substantially increase from 94.279 to 97.530 Å and from 45.777 to 47.685 Å, respectively, which signifies that the overall crystallinity of the SM-BTz-2:Y6 blend film is conducive to the formation of good vertical phase separation morphology, thus achieving higher PCE.

To dig deep into the effect of the BTz π-bridge on the charge transfer (CT) and recombination process of the active layer, we utilized femtosecond transient absorption spectroscopy to intensively study the hole transfer kinetics in the SM-BTz-2:Y6 blend film. The color plot, as shown in Fig. 8a, displays the transient absorption spectrum of the SM-BTz-2:Y6 blend films by selectively photoexciting the acceptor Y6 at 850 nm wavelength. The spectrum is mainly composed of Y6 ground state bleach (GSB) peaks at 670, 750 and 850 nm, and an excited state absorption (ESA) peak at 950 nm. The SM-BTz-2 GSB appears at 550–640 nm and rapidly decays in the first 10 ps. Additionally, Fig. 8b presents some representative transient absorption spectra of the SM-BTz-2:Y6 blends at selected delay times, which are very similar to the excited state of Y6 at 0.5 ps, implying that Y6 excitons are the dominant species for early photoexcitation. Then, as the excited state of Y6 decays, more GSB signals appear

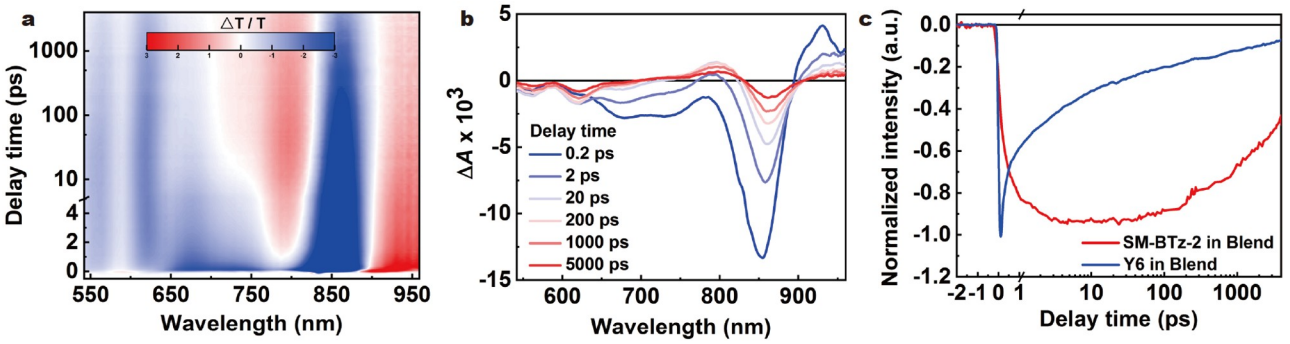

Figure 8 (a) 2D color diagram of the transient absorption spectra of the SM-BTz-2:Y6 blend film. (b) Transient absorption spectra of the SM-BTz-2:Y6 blend film at indicated delay times. (c) Kinetics traces probed at 620 nm for SM-BTz-2 and 850 nm for Y6 in the blend film.

at 560 and 620 nm, which agrees with the absorption characteristics of SM-BTz-2. Moreover, the GSB peak (at 850 nm) decaying process of the photoexcited Y6 is consistent with the SM-BTz-2 GSB (at 581 nm) rising process, substantiating the observation of hole transfer from Y6 exciton to SM-BTz-2 (Fig. 8c). The BTz π-bridge contributes to a relatively long-lived CT state in SM-BTz-2:Y6, providing sufficient charge transport and collection time to ensure the photocurrent generation of the devices, thus enabling the SM-BTz-2:Y6 device with high J_{sc} and FF.

CONCLUSION

To sum up, we synthesized two novel A-π-D-π-A-type organic SM donors SM-BTz-1 and SM-BTz-2, with BDT-TS as the electron donor core, BTz as the π-bridge units and different alkylthiosubstituted thiophene units (TS) as the end groups. Due to the electron-deficient properties of BTz, SM-BTz-1 and SM-BTz-2 possess relatively low-lying HOMO energy levels. Thus, the optimized SM-OSCs possess the V_{oc} of higher than 0.9 V and the energy losses of lower than 0.5 eV. More importantly, the SM-BTz-2:Y6 device achieved an outstanding PCE of 14.12%, which is one of the highest efficiency reported in the literature for the SM-OSCs with BTz as the π-bridge. These results indicate that the BTz unit is a promising π-bridge unit for SM-OSCs, and provide a new idea for designing photovoltaic materials with high efficiency and low energy loss.

Received 28 April 2022; accepted 27 June 2022; published online 15 September 2022

1 Sun C, Pan F, Bin H, *et al.* A low cost and high performance polymer donor material for polymer solar cells. Nat Commun, 2018, 9: 743
2 Chen X, Xu G, Zeng G, *et al.* Realizing ultrahigh mechanical flexibility and >15% efficiency of flexible organic solar cells *via* a "welding" flexible transparent electrode. Adv Mater, 2020, 32: 1908478
3 Yuan X, Sun R, Wu Y, *et al.* Simultaneous enhanced device efficiency and color neutrality in semitransparent organic photovoltaics employing a synergy of ternary strategy and optical engineering. Adv Funct Mater, 2022, 32: 2200107
4 Gu X, Zhou Y, Gu K, *et al.* Roll-to-roll printed large-area all-polymer solar cells with 5% efficiency based on a low crystallinity conjugated polymer blend. Adv Energy Mater, 2017, 7: 1602742
5 Li X, Pan F, Sun C, *et al.* Simplified synthetic routes for low cost and high photovoltaic performance n-type organic semiconductor acceptors. Nat Commun, 2019, 10: 519
6 Shi K, Qiu B, Zhu C, *et al.* Influence of altering chlorine substitution positions on the photovoltaic properties of small molecule donors in all-small-molecule organic solar cells. J Mater Chem C, 2022, 10: 2017–2025
7 Liu F, Zhou L, Liu W, *et al.* Organic solar cells with 18% efficiency enabled by an alloy acceptor: A two-in-one strategy. Adv Mater, 2021, 33: 2100830
8 Cui Y, Yao H, Zhang J, *et al.* Single-junction organic photovoltaic cells with approaching 18% efficiency. Adv Mater, 2020, 32: 1908205
9 Bao S, Yang H, Fan H, *et al.* Volatilizable solid additive-assisted treatment enables organic solar cells with efficiency over 18.8% and fill factor exceeding 80%. Adv Mater, 2021, 33: 2105301
10 Cheng Y, Huang B, Huang X, *et al.* Oligomer-assisted photoactive layers enable >18 % efficiency of organic solar cells. Angew Chem Int Ed, 2022, 61: e202200329
11 Feng W, Wu S, Chen H, *et al.* Tuning morphology of active layer by using a wide bandgap oligomer-like donor enables organic solar cells with over 18% efficiency. Adv Energy Mater, 2022, 12: 2104060
12 Zhou R, Jiang Z, Yang C, *et al.* All-small-molecule organic solar cells with over 14% efficiency by optimizing hierarchical morphologies. Nat Commun, 2019, 10: 5393
13 Xu T, Lv J, Yang K, *et al.* 15.8% Efficiency binary all-small-molecule organic solar cells enabled by a selenophene substituted sematic liquid crystalline donor. Energy Environ Sci, 2021, 14: 5366–5376
14 Zhang X, Qin L, Li Y, *et al.* High-performance all-small-molecule organic solar cells enabled by Regio-isomerization of noncovalently conformational locks. Adv Funct Mater, 2022, 32: 2112433
15 Shi K, Qiu B, Zhu C, *et al.* Effects of alkyl side chains of small molecule donors on morphology and the photovoltaic property of all-small-molecule solar cells. ACS Appl Mater Interfaces, 2021, 13: 54237–54245
16 Bin H, van der Pol TPA, Li J, *et al.* Efficient organic solar cells with small energy losses based on a wide-bandgap trialkylsilyl-substituted donor polymer and a non-fullerene acceptor. Chem Eng J, 2022, 435: 134878
17 Zhang Y, Liu D, Lau TK, *et al.* A novel wide-bandgap polymer with deep ionization potential enables exceeding 16% efficiency in ternary nonfullerene polymer solar cells. Adv Funct Mater, 2020, 30: 1910466
18 An Q, Wang J, Ma X, *et al.* Two compatible polymer donors contribute synergistically for ternary organic solar cells with 17.53% efficiency. Energy Environ Sci, 2020, 13: 5039–5047
19 An N, Cai Y, Wu H, *et al.* Solution-processed organic solar cells with high open-circuit voltage of 1.3 V and low non-radiative voltage loss of 0.16 V. Adv Mater, 2020, 32: 2002122
20 Qin Y, Zhang S, Xu Y, *et al.* Reduced nonradiative energy loss caused by aggregation of nonfullerene acceptor in organic solar cells. Adv Energy Mater, 2019, 9: 1901823
21 Zhan L, Li S, Lau TK, *et al.* Over 17% efficiency ternary organic solar cells enabled by two non-fullerene acceptors working in an alloy-like model. Energy Environ Sci, 2020, 13: 635–645
22 Ma X, Wang J, Gao J, *et al.* Achieving 17.4% efficiency of ternary organic photovoltaics with two well-compatible nonfullerene acceptors for minimizing energy loss. Adv Energy Mater, 2020, 10: 2001404
23 Guo J, Qiu B, Yang D, *et al.* 15.71% Efficiency all-small-molecule or-

ganic solar cells based on low-cost synthesized donor molecules. Adv Funct Mater, 2022, 32: 2110159
24 Guo J, Bin H, Wang W, *et al.* All-small molecule solar cells based on donor molecule optimization with highly enhanced efficiency and stability. J Mater Chem A, 2018, 6: 15675–15683
25 Chen H, Hu D, Yang Q, *et al.* All-small-molecule organic solar cells with an ordered liquid crystalline donor. Joule, 2019, 3: 3034–3047
26 Qiu B, Chen Z, Qin S, *et al.* Highly efficient all-small-molecule organic solar cells with appropriate active layer morphology by side chain engineering of donor molecules and thermal annealing. Adv Mater, 2020, 32: 1908373
27 Bin H, Yao J, Yang Y, *et al.* High-efficiency all-small-molecule organic solar cells based on an organic molecule donor with alkylsilyl-thienyl conjugated side chains. Adv Mater, 2018, 30: 1706361
28 Gao J, Ge J, Peng R, *et al.* Over 14% efficiency nonfullerene all-small-molecule organic solar cells enabled by improving the ordering of molecular donors *via* side-chain engineering. J Mater Chem A, 2020, 8: 7405–7411
29 Yang L, Zhang S, He C, *et al.* New wide band gap donor for efficient fullerene-free all-small-molecule organic solar cells. J Am Chem Soc, 2017, 139: 1958–1966
30 Liu C, Qiu N, Sun Y, *et al.* All-small-molecule organic solar cells based on a fluorinated small molecule donor with high open-circuit voltage of 1.07 V. Front Chem, 2020, 8: 329
31 Ye C, Wang Y, Bi Z, *et al.* High-performance organic solar cells based on a small molecule with thieno[3,2-*b*]thiophene as π-bridge. Org Electron, 2018, 53: 273–279
32 Zhang Z, Deng D, Li Y, *et al.* Polymerized small-molecule acceptor as an interface modulator to increase the performance of all-small-molecule solar cells. Adv Energy Mater, 2021, 12: 2102394
33 Fang J, Ye C, Wang X, *et al.* Non-fullerene organic solar cells based on a small molecule with benzo[1,2-*c*:4,5-*c*′]dithiophene-4,8-dione as π-bridge. Org Electron, 2019, 67: 175–180
34 Fan D, Fan C, Fan H, *et al.* Impact of fluorine substituted π-bridges on the photovoltaic performance of organic small-molecule donor materials. Mol Syst Des Eng, 2021, 6: 739–747
35 Wang Y, Wang Y, Zhu L, *et al.* A novel wide-bandgap small molecule donor for high efficiency all-small-molecule organic solar cells with small non-radiative energy losses. Energy Environ Sci, 2020, 13: 1309–1317
36 Xue L, Yang Y, Xu J, *et al.* Side chain engineering on medium bandgap copolymers to suppress triplet formation for high-efficiency polymer solar cells. Adv Mater, 2017, 29: 1703344
37 Bin H, Gao L, Zhang ZG, *et al.* 11.4% Efficiency non-fullerene polymer solar cells with trialkylsilyl substituted 2D-conjugated polymer as donor. Nat Commun, 2016, 7: 13651
38 Xue X, Zheng B, Zhang Y, *et al.* Two birds with one stone: High efficiency and low synthetic cost for benzotriazole-based polymer solar cells by a simple chemical approach. Adv Energy Mater, 2020, 10: 2002142
39 Bin H, Yang Y, Zhang ZG, *et al.* 9.73% Efficiency nonfullerene all organic small molecule solar cells with absorption-complementary donor and acceptor. J Am Chem Soc, 2017, 139: 5085–5094
40 Bin H, Angunawela I, Qiu B, *et al.* Precise control of phase separation enables 12% efficiency in all small molecule solar cells. Adv Energy Mater, 2020, 10: 2001589
41 Chen S, Wang Y, Zhang L, *et al.* Efficient nonfullerene organic solar cells with small driving forces for both hole and electron transfer. Adv Mater, 2018, 30: 1804215
42 Zhu C, Meng L, Zhang J, *et al.* A quinoxaline-based D-A copolymer donor achieving 17.62% efficiency of organic solar cells. Adv Mater, 2021, 33: 2100474
43 Zhou L, Meng L, Zhang J, *et al.* Introducing low-cost pyrazine unit into terpolymer enables high-performance polymer solar cells with efficiency of 18.23%. Adv Funct Mater, 2022, 32: 2109271
44 Guo J, Hu K, Qiu B, *et al.* Fine-tuning miscibility and π-π stacking by alkylthio side chains of donor molecules enables high-performance all-small-molecule organic solar cells. ACS Appl Mater Interfaces, 2021, 13: 36033–36043
45 Zhou L, Xia X, Meng L, *et al.* Introducing electron-withdrawing linking units and thiophene π-bridges into polymerized small molecule acceptors for high-efficiency all-polymer solar cells. Chem Mater, 2021, 33: 8212–8222
46 Wang Y, Qian D, Cui Y, *et al.* Optical gaps of organic solar cells as a reference for comparing voltage losses. Adv Energy Mater, 2018, 8: 1801352
47 Vandewal K, Ma Z, Bergqvist J, *et al.* Quantification of quantum efficiency and energy losses in low bandgap polymer:fullerene solar cells with high open-circuit voltage. Adv Funct Mater, 2012, 22: 3480–3490
48 Shockley W, Queisser HJ. Detailed balance limit of efficiency of p-n junction solar cells. J Appl Phys, 1961, 32: 510–519
49 Vandewal K, Benduhn J, Nikolis VC. How to determine optical gaps and voltage losses in organic photovoltaic materials. Sustain Energy Fuels, 2018, 2: 538–544
50 Ma Y, Zhou X, Cai D, *et al.* A minimal benzo[*c*][1,2,5]thiadiazole-based electron acceptor as a third component material for ternary polymer solar cells with efficiencies exceeding 16.0%. Mater Horiz, 2020, 7: 117–124
51 Rivnay J, Mannsfeld SCB, Miller CE, *et al.* Quantitative determination of organic semiconductor microstructure from the molecular to device scale. Chem Rev, 2012, 112: 5488–5519

Acknowledgements This work was supported by the National Key Research and Development Program of China (2019YFA0705900), the National Natural Science Foundation of China (51820105003, 21734008, 61904181, 52173188 and 52103243), the Key Research Program of the Chinese Academy of Sciences (XDPB13), and the Basic and Applied Basic Research Major Program of Guangdong Province (2019B030302007).

Author contributions Guo J synthesized the molecule donor materials; Guo J and Hu K performed the device fabrication and characterization of the SM-OSCs; Qiu B conducted the experiment guidance; Zhang J and Yang D were responsible for the transient absorption spectroscopy test and DFT analysis respectively; Li X, Meng L, Zhang Z and Li Y were responsible for conceptualizing the experiment, designing the experiment, and supervising the whole project.

Conflict of interest The authors declare that they have no conflict of interest.

Supplementary information Experimental data and supporting data are available in the online version of the paper.

Jing Guo received her BSc degree from Yanbian University in 2017. Now she is a jointly trained PhD candidate at the University of Chinese Academy of Sciences (UCAS) and the Institute of Chemistry, CAS (ICCAS) under the guidance of Prof. Yongfang Li. Her current research focuses on the synthesis and characterization of organic photovoltaic materials.

Beibei Qiu is currently a lecturer at Zhejiang Normal University. He received his BSc and MSc degrees from the Central South University in 2013 and 2016, respectively, and his PhD degree in 2020 from ICCAS, under the supervision of Prof. Yongfang Li. His research interests are in the fields of organic photovoltaic materials and devices.

Jinyuan Zhang received his PhD degree from the North Carolina State University (NCSU) in 2016, then he did his postdoctoral research at the Northwestern University (NU). He joined Prof. Yongfang Li's group at ICCAS as a postdoctoral fellow in 2019. His research focuses on investigating the working mechanism of organic solar cells *via* ultrafast spectroscopy.

Zhanjun Zhang received his PhD degree from Shanxi Institute of Coal Chemistry, CAS in 1999. Then he worked as a postdoctoral researcher in Prof. Shengmin Cai's group at Peking University. He became a professor of the UCAS in 2001. His research focuses on the design, synthesis and application of organic solar cell photovoltaic materials and lithium ion battery materials.

Lei Meng received his BSc degree from Shanghai Jiao Tong University in 2011, MSc degree from NU in 2012 and PhD degree from the University of California, Los Angeles (UCLA) in 2017. After graduation, he continued his postdoctoral research at UCLA. In 2018, he joined the ICCAS as a professor in the Key Laboratory of Organic Solids. His current research interest mainly focuses on organic semiconductor materials, organic solar cells and perovskite solar cells.

Yongfang Li is a professor at the ICCAS, and Soochow University. He received his PhD degree in 1986 from the Department of Chemistry, Fudan University. He joined ICCAS in 1988 and was promoted to be a professor in 1993. He was invited to be a professor at Soochow University in 2012, and was elected as a member of the CAS in 2013. His present research field is photovoltaic materials and devices for polymer solar cells.

基于苯并三氮唑π-桥单元协同高效率和低能量损失的全小分子有机太阳电池

郭静[1,2], 胡克[1,2], 邱贝贝[3*], 杨登宸[1,2], 李骁骏[1,2], 章津源[2*], 孟磊[1,2*], 张占军[1*], 李永舫[1,2,4]

摘要 降低电压损失(V_{loss})是有机光伏电池未来商业化应用面临的关键挑战之一. V_{loss}一般由活性层材料的光学带隙和器件的开路电压(V_{oc})之差定义, 而V_{oc}则由给受体之间的最低未占据分子轨(LUMO)和最高占据分子轨道(HOMO)之间的能级差决定. 本文通过引入苯并三唑(BTz) π-桥单元, 利用末端调控策略合成了两种A-π-D-π-A型小分子给体SM-BTz-1和SM-BTz-2. 结果显示, BTz π-桥单位显著降低了小分子给体的HOMO能级, 使其具有较高的V_{oc}和载流子迁移率, 实现了高效率与低能量损失(小于0.5 eV)之间的平衡. 最终, 以SM-BTz-2为给体, Y6为受体的全小分子有机太阳能电池V_{oc}为0.91 V, 短路电流密度(J_{sc})为22.8 mA cm^{-2}, 填充因子为68%, 能量转化效率为14.12%. 此外, 该工作也进一步说明了苯并三唑π-桥单元是提高载流子迁移率, 降低能量损失的有效构建单元.

